Signal Processing 138 (2017) 182–194

Contents lists available at ScienceDirect

Signal Processing

journal homepage: www.elsevier.com/locate/sigpro

Iteratively reweighted blind deconvolution for passive millimeter-wave images

Houzhang Fang[a,*], Yu Shi[b], Donghui Pan[c], Gang Zhou[d]

[a] National Laboratory of Radar Signal Processing, Xidian University, Xi'an, 710071, PR China
[b] School of Electrical and Information Engineering, Wuhan Institute of Technology, Wuhan, 430073, PR China
[c] School of Mathematical Sciences, Anhui University, Hefei, 230601, PR China
[d] State Key Laboratory of Material Processing and Die & Mould Technology, Huazhong University of Science and Technology, Wuahn, 430074, PR China

ARTICLE INFO

Article history:
Received 21 September 2016
Revised 14 January 2017
Accepted 21 January 2017
Available online 4 February 2017

Keywords:
Blind deconvolution
Passive millimeter-wave images
Iteratively reweighted
Deblurring

ABSTRACT

Passive millimeter-wave (PMMW) imaging frequently suffers from blurring and low resolution due to the diffraction limits and the long wavelengths compared with visual and infrared radiation. Moreover, the observed image is inevitably degraded by the system noise and natural clutter noise. The blur and noise limit the capability of PMMW images in practical applications. In this study, we propose an iteratively reweighted blind deconvolution method for obtaining high quality PMMW images. A weighted least-squares data-fidelity term that is robust to modeling error and a weighted bilateral total variation regularization term are incorporated into the variational blind deconvolution framework. Furthermore, we impose an appropriate smooth constraint for the point spread function of the imaging system. In addition, to improve the practicality of the method, we derive a formula to automatically update the regularization parameter from the data. Comparative experimental results on simulated and real images show that the proposed method is superior to the state-of-the-art methods in terms of both subjective measure and visual quality.

© 2017 Elsevier B.V. All rights reserved.

1. Introduction

Passive millimeter-wave (PMMW) imaging, which operates at frequencies from 30 to 300 GHz, has been attracting considerable interest in various applications [1] because it has tremendous potential for navigation, guidance, and surveillance due to its capability of penetrating fog and heavy rain and forming images at night as well as during daylight.

A main drawback to PMMW images is the poor spatial resolution. The spatial resolution of the PMMW imaging system is characterized by the wavelength and the size of the aperture of the antenna. The diffraction-limited angular resolution θ in radians of an incoherent imaging system is given by $\theta = 1.22\lambda/D$, where D is the aperture size and λ is the wavelength of the radiation. PMMW radiation has a longer wavelength than the visual and infrared radiation. Moreover, the aperture of the antenna must be comparably larger to obtain an acceptable spatial resolution. However, the use of very large apertures is often strictly limited because of the platform constraints and requirements in many practical applications. Thus, the acquired images are highly blurred and the spatial resolution is low. In addition, the observed image is inevitably degraded by the system noise and natural clutter noise. Therefore, more efficient and economical ways, such as image restoration algorithms [2–5] and super resolution techniques [6], are essential to obtain high-quality images for use in many practical applications such as target detection, identification, and surveillance.

Many image enhancement techniques [2,3,6–10] have been developed to improve the spatial resolution of PMMW images. In these methods, the blind image deconvolution methods [2,3,8,9,11] are typically utilized to improve the resolution of PMMW images. However, blind image deconvolution is known to be a severely ill-posed inverse problem [12,13]. Therefore, the prior knowledge is necessarily introduced in order to obtain a reasonable and stable solution. In [8,11], the authors assumed that the point spread function (PSF) of the PMMW imaging system has a parametric form and employed the Gaussian-like shape function to approximate the parametric model, and then Fourier-wavelet regularized deconvolution and the wavelet based maximum entropy method are used to restore the image. In [3,14], we also constructed a joint blind deconvolution algorithm to simultaneously estimate the image and the parameter of the PSF by assuming that the PSF of the PMWW imaging system can be approximated

* Corresponding author: Tel.: +86 29 88201400
E-mail addresses: houzhangfang@xidian.edu.cn (H. Fang), shiyu0125@163.com (Y. Shi), dhpan@ahu.edu.cn (D. Pan), visualab@163.com (G. Zhou).

http://dx.doi.org/10.1016/j.sigpro.2017.01.021
0165-1684/© 2017 Elsevier B.V. All rights reserved.

with the Gaussian shape function, and framelet transform and total variation regularization are incorporated into the algorithm in order to improve image restoration performance. The methods presented in [3,11] improved the spatial resolution of the PMMW images. However, the parametric model for the PSF of the PMMW imaging system is limited in practical applications because this approximation model cannot fit real cases well. In [9], the authors proposed a joint iterative blind deconvolution algorithm for compressive sensing based imaging systems and imposed a variant of the ℓ_p quasi-norm as a regularization term for the image. The authors in [9,15] found that the PSF of the PMMW imaging system is smooth. The results presented in [9] illustrated that the smoothing model is reasonable. The image noise in [9] is also suppressed well and large scale structure details are restored efficiently. In fact, the smoothness modeling for the PSF of the PMMW imaging system (such as in [9]) can be regarded as a generalization of the Gaussian-like shape and Gaussian shape model (such as in [3,11]) because the latter kind of PSF also exhibits smoothness.

Recently, a multi-scale framework has also been utilized to improve the accuracy of the PSF estimation [16,17]. This multi-resolution coarse-to-fine mechanism can avoid the solution by the blind deconvolution algorithm falling into a local minimum and reduce the computational time. Levin et al. in [17] argued that a general image prior is vital in the maximum a posterior (MAP) blind deconvolution framework. Since a normalized sparsity measurement of ℓ_1/ℓ_2 norm is beneficial for a sparse solution. In [16], the ℓ_1/ℓ_2 norm was adopted for image deblurring and the image deconvolution is performed in the sparse derivative domain. Both Krishnan et al. and Levin et al. advocated estimating the PSF alone within a multi-scale framework followed by performed a non-blind deconvolution to restore the image.

In the PMMW imaging system, in general, the PSF of the imaging system cannot be accurately known in advance and its estimation is essential for the accurate restoration of high resolution images. In this study, we present a blind deconvolution method in the variational regularization framework to estimate both the image and the PSF by using a multi-scale framework. We impose the smooth prior constraint for the PSF of the PMMW imaging system using the ℓ_2 norm of the PSF under the Laplace operator. As pointed out in [6,18], image deconvolution is not a trivial problem in the presence of noise and the noise handling is crucial in blind deconvolution tasks. To better suppress the strong noise in the PMMW images, we incorporate a reweighted data-fidelity term and a reweighted adaptive bilateral total variation regularization into the variational framework. The introduction of the adaptive data-fidelity term weight makes the constructed blind image deconvolution algorithm more robust to the modeling error (such as the mixed noise [6]). We also derive the automatic updating formula for the regularization parameters, making the method practically promising.

The paper is organized as follows. In Section 2, we present the proposed algorithm. In Section 3, numerical experiments are given to demonstrate the effectiveness of the proposed model. Finally, some concluding remarks are given in Section 4.

2. The proposed method

Generally, a discretized formulation of PMMW imaging is modelled in the form of a two dimensional matrix-vector:

$$\mathbf{y} = \mathbf{H}\mathbf{x} + \mathbf{n} = \mathbf{X}\mathbf{h} + \mathbf{n}, \tag{1}$$

where **y, h, x**, and **n** denote the observed image, PSF of the imaging system, high-resolution image, and noise, respectively. $\mathbf{H} \in \mathbb{R}^{N\times N}$ represents the block-circulant blurring matrix notation of the convolution of the PSF $\mathbf{h} \in \mathbb{R}^N$. Similarly, $\mathbf{X} \in \mathbb{R}^{N\times N}$ denotes the block-circulant matrix formed from the image $\mathbf{x} \in \mathbb{R}^N$ (N is the number of pixels of the image.).

We solve the restoration problem (1) as a joint minimization problem within a variational regularization framework. Thus, the aim of the blind image deconvolution is to recover the PSF and the unknown image simultaneously by using the available degraded observation as the minimizer of the objective function

$$J(\mathbf{x}, \mathbf{h}) = \frac{1}{2}\|\mathbf{H}\mathbf{x} - \mathbf{y}\|_2^2 + \lambda R(\mathbf{x}) + \gamma Q(\mathbf{h}), \tag{2}$$

where the first term is the data-fidelity term, which measures the fidelity to the observation data. The $R(\mathbf{x})$ and $Q(\mathbf{h})$ are the regularization terms on the image and on the PSF, respectively. λ and γ are the regularization parameters.

2.1. The construction of the data-fidelity term

It is often the case that the noise in real PMMW imaging applications does not always follow Gaussian noise distribution perfectly. As pointed out in [6], the observed image can be distorted by mixed noise (such as salt-pepper and Poisson noises) in real applications. In this case, the observation data are not consistent with the forward model (1), which means that a small error perturbation in the observation data due to the noise can cause a severe degradation in the resulting estimation. Then, blind image deconvolution can be severely degraded and the resulting restored image may be unrecognizable. To enhance the robustness of the algorithm to model mismatch, we consider modifying the data-fidelity term by introducing a adaptive weight, which makes the blind deconvolution algorithm robust to modeling errors and outliers. Then, the energy function (2) can be further written as

$$J(\mathbf{x}, \mathbf{h}) = \frac{1}{2}\|\mathbf{W}_F^{1/2}(\mathbf{H}\mathbf{x} - \mathbf{y})\|_2^2 + \lambda R(\mathbf{x}) + \gamma Q(\mathbf{h}), \tag{3}$$

where $\mathbf{W}_F \in \mathbb{R}^{N\times N}$ is the diagonal weight matrix, which is determined based on the residual error $\mathbf{r} = (r_i) = \mathbf{H}\mathbf{x} - \mathbf{y}$. We define the weight function vector $\mathbf{w} = [w_1(\mathbf{r}|\sigma_1), \ldots, w_N(\mathbf{r}|\sigma_1)]^T$, where each diagonal element w_i in the weight $\mathbf{W}_F$ along the diagonals is given by

$$w_i = \begin{cases} 1, & \text{if } |r_i| \le c\sigma_1, \\ c\sigma_1 \exp(-cr_i^2), & \text{otherwise,} \end{cases} \tag{4}$$

where σ_1 is the noise standard deviation, which is adopted to discriminate the inliers and outliers with a fixed constant c. In our implementation, $c = 2$ yields a correct classification more than 95% of the time for the true inliers observations assuming they follow a Gaussian distribution. Observations that are not explained as inliers are weighted by the inverse of the exponent of their absolute residual error resulting in a lower confidence weight. The noise standard deviation σ_1 is estimated based on the median absolute deviation of the residual error **r** and computed by

$$\sigma_1 = 1.48 \underset{i=1,\ldots,N}{\text{median}}\big(|r_i - \text{median}(\mathbf{r}|\mathbf{w})|\big|\mathbf{w}\big), \tag{5}$$

where median $(\mathbf{r}|\mathbf{w})$ is the weighted median of the residual **r** under the weight **w**. The reweighted technique in the data term [19] has been adopted, but the constructed weight based on the simple piecewise truncated function is not very effective. The refined weight estimation based on the median absolute deviation of the residual error is also adopted for image deconvolution [20] and superresolution [21], and the achieved results are competitive and promising for real-world applications.

2.2. The construction of the regularization terms

The bilateral total variation (BTV) operator is first introduced as a regularization term for image superresolution [22], which

preserves more edges and is easy to implement. The BTV regularization term by combining the total variation and the bilateral filter is given by

$$R_{\mathrm{BTV}}(\mathbf{x}) = \sum_{l=-P}^{P}\sum_{m=0}^{P} c_0^{|m|+|l|}\|\mathbf{x}-\mathbf{S}_h^l\mathbf{S}_v^m\mathbf{x}\|_1, \tag{6}$$

where $l+m\geq 0$, $P\geq 1$. $\mathbf{S}_h^l$ and $\mathbf{S}_v^m$ are the shift matrices operators representing l and m pixels shift in horizontal and vertical directions, respectively. c_0 $(0<c_0<1)$ is the weighting constant. For convenience of mathematical expression, (6) is further converted into the following form by a new linear transform matrix $\mathbf{T}=\left[\mathbf{S}^{-P,-P}\mathbf{S}^{-P+1,-P}\ldots\mathbf{S}^{P,P}\right]^T\in\mathbb{R}^{N'\times N}$

$$R_{\mathrm{BTV}}(\mathbf{x}) = \|\mathbf{T}\mathbf{x}\|_1, \tag{7}$$

where $\mathbf{S}^{m,n}=c_0^{|m|+|n|}(\mathbf{I}-\mathbf{S}_h^l\mathbf{S}_v^m)$ and $N'=(2P+1)^2N$. Inspired by the success of the reweighting strategy [20,21], we can incorporate a similar reweighted strategy for the image into our blind deconvolution framework

$$R_{\mathrm{BTV}}(\mathbf{x}) = \|\mathbf{W}_R\mathbf{T}\mathbf{x}\|_1, \tag{8}$$

where $\mathbf{W}_R\in\mathbb{R}^{N'\times N'}$ is the diagonal weighting matrix. The reweighting strategy under ℓ_2 norm can be used for image deconvolution [19]. One aim of utilizing the reweighting strategy under ℓ_1 norm is to promote the sparsity of the solution [23], as it was commonly considered that an image prior which encourages strong sparsity in gradients yields a better performance in blind image deconvolution [24]. On the other hand, the incorporation of the adaptive weight renders the algorithm a locally adaptive ability to better preserve the edges and detail information. The construction of the weight $\mathbf{W}_R$ is similar to that of the weight $\mathbf{W}_F$ and its computation is based on the coefficients $\mathbf{z}=\mathbf{T}\mathbf{x}$ of the image under the bilateral total variation operation. Each element u_i of the weight vector $\mathbf{u}=[u_1,u_2,\ldots,u_{N'}]^T$ in the weight $\mathbf{W}_R$ along the diagonals is given by

$$u_i(\mathbf{z}|\sigma_2) = \begin{cases} 1, & \text{if } |(\mathbf{T}\mathbf{x})_i|\leq c\sigma_2,\\ \frac{\sqrt{c\sigma_2}}{2\sqrt{|(\mathbf{T}\mathbf{x})_i|}}, & \text{otherwise,}\end{cases} \tag{9}$$

σ_2 is used to discriminate flat and discontinuities regions with a constant $c=2$ analogous to the observation weights. A constant weight is adopted for small $|(\mathbf{T}\mathbf{x})_i|$ corresponding to flat regions affected by residual noise. A small weight is utilized for large $|(\mathbf{T}\mathbf{x})_i|$ that is chosen to be proportional to the inverse of the magnitude of the transformed image in order to impose less penalization on the edge and discontinuities region. σ_2 is the adaptive parameter and estimated from the coefficients $\mathbf{T}\mathbf{x}$

$$\sigma_2 = \underset{i=1,\ldots,N'}{\mathrm{median}}\Big(\big|(\mathbf{T}\mathbf{x})_i-\mathrm{median}(\mathbf{T}\mathbf{x}|\mathbf{u})\big|\Big|\mathbf{u}\Big). \tag{10}$$

In [25], the weighted anisotropic TV regularization term considering the directions features has been adopted to improve the performance of image deconvolution. The iteratively reweighted technique was also used in [26,27] for improving image restoration performance.

As for the regularization of the PSF, we adopt the smoothing constraint

$$Q(\mathbf{h}) = \|\Gamma\mathbf{h}\|_2^2, \tag{11}$$

where Γ is the discrete matrix realization of the Laplacian kernel

$$\Gamma_{\mathrm{kernel}} = \begin{bmatrix} 0 & -1 & 0\\ -1 & 4 & -1\\ 0 & -1 & 0\end{bmatrix}. \tag{12}$$

The rationale behind the choice of the smoothness prior is that the PSF of PMMW imaging system is smooth, which has already been clarified in the introduction. With this model, we will be able to estimate the discrete values of the overall PSF instead of a simple parametric form. This choice also provides us with a convenient numerical implementation.

2.3. Optimization of the image and the PSF

Combing the models in (3), (8), and (11), we have the final blind image deconvolution model

$$J(\mathbf{x},\mathbf{h}) = \frac{1}{2}\|\mathbf{W}_F^{1/2}(\mathbf{H}\mathbf{x}-\mathbf{y})\|_2^2+\lambda\|\mathbf{W}_R\mathbf{T}\mathbf{x}\|_1+\gamma\|\Gamma\mathbf{h}\|_2^2. \tag{13}$$

A. Restoration of the image $\boldsymbol{x}$

Finding directly closed form solutions for the minimization of the image restoration in (13) is very difficult because the data-fidelity term contains the adaptive weight $\mathbf{W}_F$ and the regularization term $\|\mathbf{W}_R\mathbf{T}\mathbf{x}\|_1$ on the image is inseparable and non-differentiable, which precludes the application of standard unconstrained approaches. To overcome the latter difficulties, we apply to (8) the smooth approximation

$$R_{\mathrm{BTV}}(\mathbf{x}) = \|\mathbf{W}_R\mathbf{T}\mathbf{x}\|_1 \approx \sum_{i=1}^{N'} u_i\sqrt{(\mathbf{T}\mathbf{x})_i^2+\epsilon}. \tag{14}$$

This is a very standard approximation to the ℓ_1 norm regularization [28]. This approximation is continuous and differentiable and approximates $\|\mathbf{W}_R\mathbf{T}\mathbf{x}\|_1$ for small ϵ. The final minimization problem on the image $\mathbf{x}$ can be written as

$$\min_{\mathbf{x}}\frac{1}{2}\|\mathbf{W}_F^{1/2}(\mathbf{H}\mathbf{x}-\mathbf{y})\|_2^2+\lambda\sum_{i=1}^{N'} u_i\sqrt{(\mathbf{T}\mathbf{x})_i^2+\epsilon}. \tag{15}$$

The gradient of the above objective function with respect to the image $\mathbf{x}$ for each element is

$$\left(\mathbf{H}^T\mathbf{W}_F(\mathbf{H}\mathbf{x}-\mathbf{y})\right)_i+\lambda u_i\mathbf{T}^T\frac{(\mathbf{T}\mathbf{x})_i^2}{\sqrt{(\mathbf{T}\mathbf{x})_i^2+\epsilon}}, \tag{16}$$

where T denotes the transpose of the matrix. The smooth approximation to $\|\mathbf{W}_R\mathbf{T}\mathbf{x}\|_1$ allows us to find a numerical solution by the scaled conjugate gradient method [29] which is very efficient. Other numerical techniques, such as the preconditioning conjugate gradient can also be utilized.

B. Estimation of the PSF $\boldsymbol{h}$

The minimization problem on the PSF is

$$\min_{\mathbf{h}}\frac{1}{2}\|\mathbf{W}_F^{1/2}(\mathbf{X}\mathbf{h}-\mathbf{y})\|_2^2+\gamma\|\Gamma\mathbf{h}\|_2^2. \tag{17}$$

The gradient of the above objective function with respect to the PSF $\mathbf{h}$ is

$$\frac{\partial J(\mathbf{x},\mathbf{h})}{\partial\mathbf{h}} = \mathbf{X}^T\mathbf{W}_F(\mathbf{X}\mathbf{h}-\mathbf{y})+\gamma\Gamma^T\Gamma\mathbf{h}. \tag{18}$$

We find the numerical solution to the PSF by using the scaled conjugate gradient method [29]. Similarly, the conjugate gradient or preconditioning conjugate gradient, can also be used.

2.4. Selection of the regularization parameters

The regularization parameter plays an important role in the variational regularization framework by controling the tradeoff between the data-fidelity term and regularization term. Here, we provide an approximation way to automatically select the regularization parameters λ and γ.

A. Estimation of the image regularization parameter λ

By Eq. (8), we model the coefficients of the image under the bilateral total variation operation as samples from a Laplacian distribution with zero mean. Note that this assumption may not coincide with real situations because the coefficients are statistically dependent. However, this assumption gives an approximative way to choose the regularization parameter. We set the coefficients $\boldsymbol{\theta} := \mathbf{W}_R\mathbf{T}\mathbf{x}$. The Laplacian distribution for the coefficients $\boldsymbol{\theta}$ is defined as

$$p(\theta|\sigma_\theta) = \left(\frac{c_1}{\sqrt{2}\sigma_\theta}\right)^{-\#\theta} \exp\left(-c_1\sqrt{2}\frac{\|\theta\|_1}{\sigma_\theta}\right), \tag{19}$$

where $\sigma_{\boldsymbol{\theta}}$ is a scale parameter and $\#\theta$ is the number of coefficients $\boldsymbol{\theta}$. c_1 is a constant. The maximum likelihood (ML) estimation $\sigma_\theta^{\mathrm{ML}}$ of $\sigma_{\boldsymbol{\theta}}$ can be written as

$$\begin{aligned}\sigma_\theta^{\mathrm{ML}} &= \arg\max_{\sigma_\theta}\{p(\theta|\sigma_\theta)\} \\ &= \arg\min_{\sigma_\theta}\left\{\#\sigma_\theta \ln\left(\sqrt{2}\sigma_\theta\right) + c_1\sqrt{2}\|\theta\|_1/\sigma_\theta\right\}.\end{aligned} \tag{20}$$

We then have

$$\sigma_\theta^{\mathrm{ML}} = \frac{c_1\sqrt{2}\|\theta\|_1}{\#\sigma_\theta}. \tag{21}$$

Suppose that $p(\mathbf{x})$ and $p(\mathbf{x}|\mathbf{y})$ are the prior and posterior probability distributions, respectively. By Bayes' formula $p(\mathbf{x}|\mathbf{y}) = p(\mathbf{y}|\mathbf{x})p(\mathbf{x})/p(\mathbf{y})$, we obtain the MAP estimation

$$\begin{aligned}\hat{\mathbf{x}} &= \arg\max_{\mathbf{x}}\{p(\mathbf{x}|\mathbf{y})\} \\ &= \arg\max_{\mathbf{x}}\{\ln p(\mathbf{y}|\mathbf{x}) + \ln p(\mathbf{x})\}.\end{aligned} \tag{22}$$

We know that $p(\mathbf{x}) = p(\mathbf{W}_R\mathbf{T}\mathbf{x}) = p(\theta|\sigma_\theta)$. Thus, replacing $p(\boldsymbol{\theta}|\sigma_{\boldsymbol{\theta}})$ in (16) with (13), we have

$$\hat{\mathbf{x}} = \arg\min_{\mathbf{x}}\left\{-\ln p(\mathbf{y}|\mathbf{x}) + c_1\sqrt{2}\|\mathbf{W}\mathbf{T}\mathbf{x}\|_1/\sigma_\theta\right\}. \tag{23}$$

By comparing the model in (13) with the model in (23), we can arrive at the conclusion that λ should be proportional to $c_1/\sigma_{\boldsymbol{\theta}}$, where $\sigma_{\boldsymbol{\theta}}$ is a scale parameter of the coefficients $\boldsymbol{\theta}$. As pointed out in [30,31], the image regularization parameter λ is also proportional to the data-fidelity term $\|\mathbf{W}_F^{1/2}(\mathbf{H}\mathbf{x}-\mathbf{y})\|_2^2$. Then, we propose the following approximative selection of the regularization parameter

$$\lambda = c_1\|\mathbf{W}_F^{1/2}(\mathbf{H}\mathbf{x}-\mathbf{y})\|_2^2/\|\mathbf{W}_R\mathbf{T}\mathbf{x}\|_1. \tag{24}$$

In our experiments, satisfactory results are obtained for $c_1 \in [3, 5]$.

B. Estimation of the PSF regularization parameter γ

Joint MAP is a Bayesian estimator that jointly estimates the PSF and the parameters [32,33]. Assume that $p(\mathbf{y}|\mathbf{x}, \mu)$ and $p(\mathbf{x}|\tau)$ are the likelihood density and the PSF prior density, respectively. We model $p(\mathbf{y}|\mathbf{x}, \mu)$ and $p(\mathbf{x}|\tau)$ as the following Gaussian densities

$$\begin{aligned}p(\mathbf{y}|\mathbf{x}, \mu) &= \frac{1}{(2\pi\mu)^{N/2}}\exp\left(-\frac{\|\mathbf{W}_F^{1/2}(\mathbf{H}\mathbf{x}-\mathbf{y})\|_2^2}{2\mu}\right), \\ p(\mathbf{x}|\tau) &= \frac{1}{(2\pi\tau)^{M/2}}\exp\left(-\frac{\|\Gamma\mathbf{h}\|_2^2}{2\tau}\right),\end{aligned} \tag{25}$$

where μ is the hyperparameter of the data density and is the variance of the data error in this work. τ is the hyperparameter of the PSF prior. M is the number of pixels of the PSF. In the MAP estimation, the hyperparameters are assumed to have fixed values [33]. In this case, the regularization parameter can be achieved as $\gamma = \mu/\tau$.

In this work, we employ flat improper uniform hyperpriors on μ and τ, that is, we utilize $p(\mu)\propto$const and $p(\tau)\propto$const. Therefore, the joint MAP estimation with these hyperpriors becomes

$$\hat{\mathbf{h}}, \hat{\mu}, \hat{\tau} = \arg\min_{\mathbf{h},\mu,\tau}\frac{\|\mathbf{W}_F^{1/2}(\mathbf{H}\mathbf{x}-\mathbf{y})\|_2^2}{2\mu} + \frac{N}{2}\ln\mu + \frac{\|\Gamma\mathbf{h}\|_2^2}{2\tau} + \frac{M}{2}\ln\tau. \tag{26}$$

We adopt the classical joint MAP estimation for the PSF and hyperparameters [32,33] and the final updating equation for the regularization parameter is

$$\gamma = \frac{M}{N}\frac{\|\mathbf{W}_F^{1/2}(\mathbf{H}\mathbf{x}-\mathbf{y})\|_2^2}{\|\Gamma\mathbf{h}\|_2^2}. \tag{27}$$

2.5. Edge emphasizing smoothing and multi-scale framework

Many recent work [34–36] on blind image deconvolution illustrated that the edge emphasizing pre-smoothing operation in the stage of the estimation of the PSF favors an accurate estimation of the PSF. In general, the goal of the edge emphasizing operation is to detect and refine the large-scale step sharp edges. In this study, we adopt the ℓ_0 norm based gradient minimization [37] to enhance the large-scale edges and globally remove most of the low-amplitude structures and suppress the adverse effect of the strong noise pixels in the estimation of the PSF.

Blind image deconvolution of the image and the PSF is a non-convex problem, and hence, the solution is easy to fall into the local minimum. A multi-scale coarse-to-fine scheme is successfully employed to overcome this and it has been validated by current blind deconvolution algorithms [16,17]. At each level in the multi-scale pyramid, the initial image and PSF in finer levels are obtained from the upsampled image and PSF in lower levels. In the coarsest level, we use a Gaussian kernel as an initial blur kernel. The kernel size at the coarsest level is 3×3 and the upscaling factor is $\sqrt{2}$.

Recent researches on joint iterative blind deconvolution [38,39] have demonstrated that blind deconvolution algorithms that simultaneously estimate the image and PSF using projecting alternating minimization can converge to a satisfactory result. A critical step to success for blind deconvolution is to separate the normalization and the positivity constraints on the PSF from the minimization step. Specifically, after updating $\mathbf{x}$ and $\mathbf{h}$ at each alternating minimization iteration, we impose the positivity, normalization, and the centralization constraints on the PSF

$$\mathbf{h} = \max(\mathbf{h}, 0), \quad \mathbf{h} = \mathbf{h}/\|\mathbf{h}\|_1, \quad \mathbf{h} = \mathrm{centralize}(\mathbf{h}), \tag{28}$$

where centralize($\mathbf{h}$) means that we shift the PSF to the location of the centroid. For a spatial domain PSF $h(x, y)$, the location of the centroid is the point $(\Sigma_x x\Sigma_y h,\ \Sigma_y y\Sigma_x h)$.

Taking all the above into account, we get the complete iteration algorithm for iteratively reweighted blind image deconvolution and it is summarized below in Algorithm 1.

In Algorithm 1, k is the number of iterations. $\mathbf{x}^{(k)}$ denotes the result of the kth iteration. K_{MaxIter} represents the maximum iteration number. In order to apply the scaled conjugate gradient method to the minimization problems (15) and (17), we invoke the NETLAB toolbox which is freely available from the Internet [40].

3. Experimental results and discussion

In this section, we demonstrate the performance of the proposed algorithm with both simulated and real data sets. As shown in Fig. 1, the ten test images Cameraman, Lena, Satellite, Boat, Bridge, Goldhill, House, Jet, Pepper, and color House are used for simulation. All of the test images were normalized to between 0 and 1. In using the algorithm, we set $P = 2$, $c_0 = 0.6$, and $\epsilon = 0.0001$. In our implementation, the maximum iteration number K_{MaxIter} of Algorithm 1 is set to be 100.

We compare the proposed algorithm with the methods of Levin et al. [17] and Krishnan et al. [16], both of which are performed within a multi-scale framework. Levin et al.'s algorithm is a very representative method in blind image deconvoloution, which is

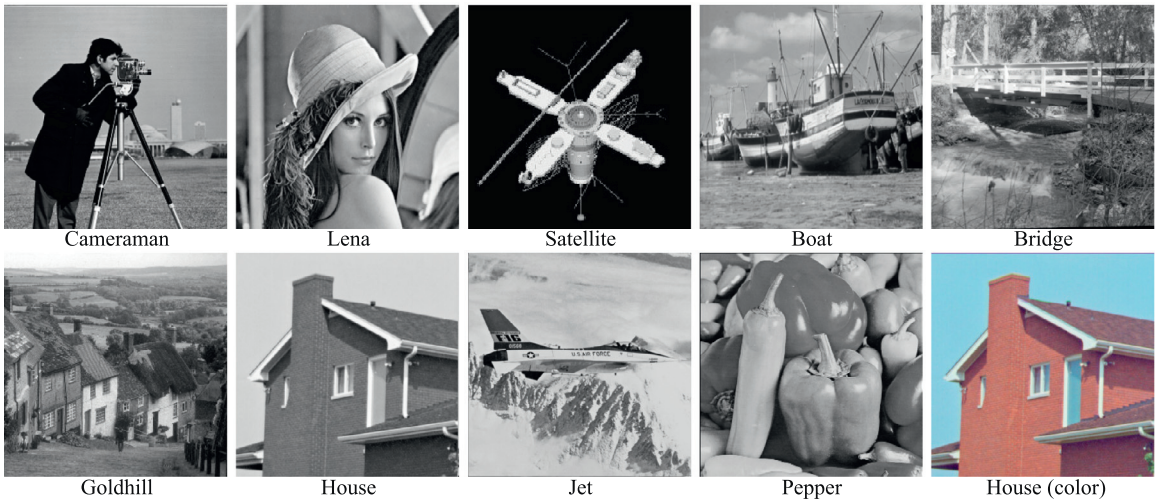


Fig. 1. Ten test images for simulation. Top (from left to right): Cameraman, Lena, Satellite, Boat, and Bridge. Bottom (from left to right): Goldhill, House, Jet, Pepper, and color House.

Algorithm 1 Iteratively Reweighted Blind Deconvolution Algorithm.

Input: The observed image $\mathbf{y}$, $S :=$ #of Scales.
Initialization: $\mathbf{x}^{(0)} = \mathbf{y}$, PSF $\mathbf{h}^{(0)}$, tol $= 0.0001$, $\epsilon = 0.0001$. Initialize the weight $\mathbf{w}^{(0)}$ with $\mathbf{1}$.
for $s = 1$ to S **do**
  Rescale $\mathbf{y}$, $\mathbf{x}^{(k)}$, and $\mathbf{h}^{(k)}$;
  for $k = 0$ to K_{MaxIter} and $\|\mathbf{x}^{(k)} - \mathbf{x}^{(k+1)}\|_2 / \|\mathbf{x}^{(k)}\|_2 <$ tol **do**
    Update $k := k + 1$.
    % Updating procedure for $\mathbf{x}^{(k)}$
    Compute the weight $\mathbf{W}_F$ based on Eq. (4);
    Compute the weight $\mathbf{W}_R$ based on Eq. (9);
    Compute the parameter $\lambda^{(k)}$ based on Eq. (24);
    Restore the image $\mathbf{x}$ based on (15) and (16) with scaled conjugate gradient method;
    % Updating procedure for $\mathbf{h}^{(k)}$
    Compute $\gamma^{(k)}$ based on Eq. (27);
    Compute the edge emphasizing pre-smoothing image based on ℓ_0 gradient minimization;
    Estimate the PSF $\mathbf{h}$ based on (17) and (18) with scaled conjugate gradient method;
    % Constraints on $\mathbf{h}^{(k)}$
    Impose the constraints on $\mathbf{h}^{(k)}$ based on (28);
  end for
end for

based on a variational Bayesian inference framework without parameter adjustment and is regarded as a benchmark method for comparison. Krishnan et al.'s method [16] adopted a normalized sparsity measurement for the image and a sparse measurement for the PSF, which can be used for natural image restoration.

A. Simulated experiments and discussion

The images were degraded by the size 11 × 11 Gaussian blur kernel with the standard deviation of 2.1. Then, the blurred images were contaminated by Gaussian noise with three noise standard deviations: 0.005, 0.01, and 0.03. We employ the MATLAB function fspecial() to simulate the PSF. For the improvement in the restored image quality to be measured, the peak signal-to-noise ratio (PSNR) and Structural Similarity Index Measure (SSIM) [41] are employed to quantitatively evaluate the quality of the observed degraded image $\mathbf{y}$ and of the restored image $\mathbf{x}$. PSNR is calculated by $10\log(N/\|\mathbf{x} - \hat{\mathbf{x}}\|^2)$ where $\mathbf{x}$ and $\hat{\mathbf{x}}$ denote the original and the restored image, respectively. N denotes the total number of image pixels. The quality of the estimated PSF is evaluated by the normalized mean squared error (NMSE) between the true PSF $\mathbf{h}$ and estimated PSF $\hat{\mathbf{h}}$: $\text{NMSE}(\hat{\mathbf{h}}) = \|\mathbf{h} - \hat{\mathbf{h}}\|_2^2 / \|\mathbf{h}\|_2^2$.

Table 1
PSNR (dB)/SSIM comparisons of three methods using nine images for Gaussian blur with size 11 × 11 and standard derivation of 2.1 and three Gaussian noise standard deviation.

Image	Noise std.	Observed	Krishnan [16]	Levin [17]	Proposed
Cameraman	0.005	21.64/0.6986	22.44/0.7625	23.06/0.7702	**23.62/0.7860**
	0.01	21.59/0.6641	22.36/0.7436	23.17/0.7706	**23.35/0.7854**
	0.03	21.09/0.4620	19.47/0.3001	22.78/0.7078	**22.84/0.7608**
Lena	0.005	22.76/0.7176	23.96/0.7960	25.27/0.8090	**26.19/0.8294**
	0.01	22.70/0.6946	23.79/0.7789	24.86/0.7995	**26.02/0.8157**
	0.03	22.08/0.5466	20.97/0.5283	24.41/0.7507	**25.26/0.7755**
Satellite	0.005	22.14/0.7452	23.44/0.8324	23.78/0.8343	**24.20/0.8346**
	0.01	22.09/0.6707	23.31/0.7938	23.61/0.8152	**24.14/0.8217**
	0.03	21.55/0.3636	21.14/0.4337	23.06/0.6820	**23.66/0.7837**
Boat	0.005	23.84/0.6697	25.60/0.7605	23.25/0.7070	**25.70/0.7631**
	0.01	23.75/0.6462	25.38/0.7539	22.68/0.6780	**25.84/0.7612**
	0.03	22.89/0.4968	21.35/0.4799	24.10/0.6863	**25.00/0.7029**
Bridge	0.005	21.89/0.4943	23.02/0.6208	21.67/0.5578	**24.11/0.6551**
	0.01	21.83/0.4870	22.89/0.6130	22.31/0.5753	**23.95/0.6309**
	0.03	21.33/0.4259	19.18/0.3871	21.58/0.5343	**22.86/0.5402**
Goldhill	0.005	23.40/0.5717	23.97/0.6717	23.19/0.6353	**24.91/0.6747**
	0.01	23.31/0.5585	23.79/0.6615	23.29/0.6215	**24.96/0.6635**
	0.03	22.51/0.4568	18.13/0.2965	22.82/0.5911	**24.76/0.6099**
House	0.005	25.15/0.7642	26.75/0.8259	24.00/0.7860	**27.78/0.8264**
	0.01	25.03/0.7295	26.52/0.8071	26.93/0.8192	**28.34/0.8260**
	0.03	23.91/0.5154	21.50/0.4189	26.18/0.7645	**28.05/0.8139**
Jet	0.005	25.40/0.8956	27.37/0.9483	26.20/0.9335	**28.83/0.9595**
	0.01	25.29/0.8866	27.14/0.9341	27.28/0.9404	**28.51/0.9500**
	0.03	24.25/0.8056	21.11/0.6345	26.28/0.8719	**26.45/0.9008**
Pepper	0.005	22.83/0.7773	23.42/0.8337	23.29/0.8200	**25.20/0.8559**
	0.01	22.76/0.7511	23.26/0.8138	22.98/0.8072	**25.19/0.8551**
	0.03	22.13/0.5755	20.56/0.5014	21.55/0.7194	**24.08/0.8079**

Table 1 lists the PSNR and SSIM values of the degraded images and of the ten test images calculated by the three methods. It can be seen that the proposed method has achieved the highest PSNR and SSIM among the three methods in Table 1. The proposed algorithm has an obvious improvement in PSNR and SSIM over the other methods when the noise intensity increases.

Table 2 lists the NMSE values of the estimated PSFs by the three methods for the images Cameraman, Lena, and Satellite. We can

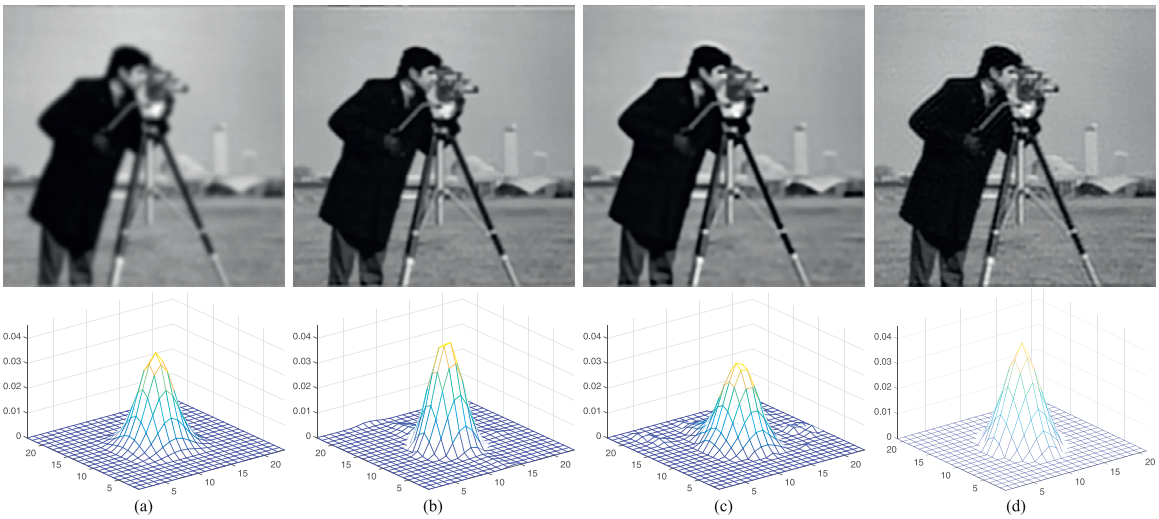


Fig. 2. Blind deconvolution results for the Cameraman image with the noise level = 0.005. (a) Image blurred by fspecial ('gaussian',11,2.1) and contaminated by Gaussian noise with standard deviation 0.005. Deconvolution results achieved using (b) Krishnan et al.'s algorithm [16], (c) Levin et al.'s algorithm [17], (d) our method. The bottom line: the original PSF and the estimated PSFs by three methods.

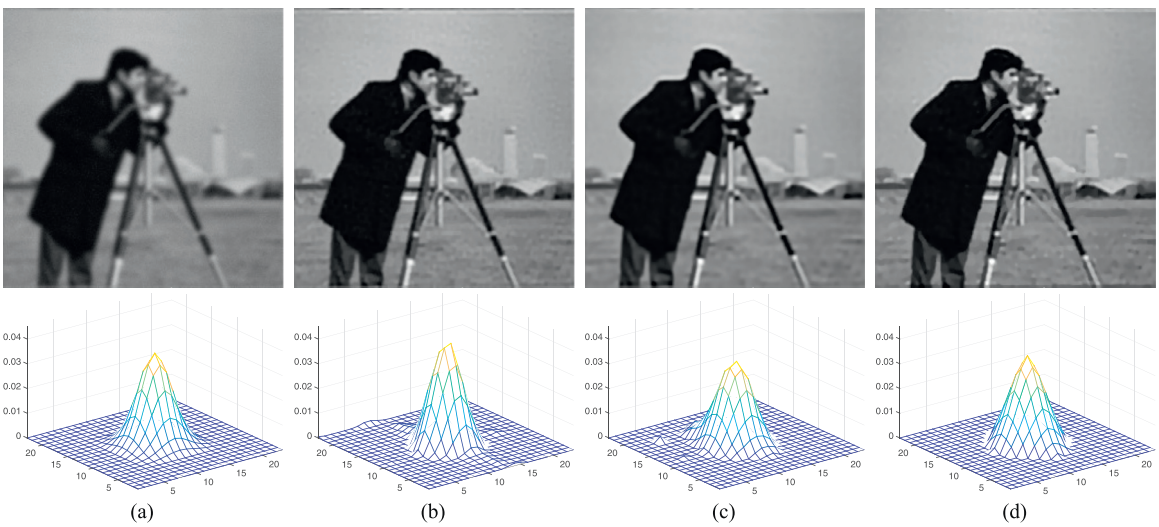


Fig. 3. Blind deconvolution results for the Cameraman image with the noise level = 0.01. (a) Image blurred by fspecial ('gaussian',11,2.1) and contaminated by Gaussian noise with standard deviation 0.01. Deconvolution results achieved using (b) Krishnan et al.'s algorithm [16], (c) Levin et al.'s algorithm [17], (d) our method. The bottom line: the original PSF and the estimated PSFs by three methods.

Table 2
NMSE comparisons of the estimated PSFs by three methods using three images for Gaussian blur with size 11 × 11 and standard derivation of 2.1 and three Gaussian noise standard deviation.

Image	Noise std.	Krishnan [16]	Levin [17]	Proposed
Cameraman	0.005	0.0644	0.0361	**0.0153**
	0.01	0.0672	0.0602	**0.0221**
	0.03	0.1172	0.0983	**0.0146**
Lena	0.005	0.0897	0.0398	**0.0140**
	0.01	0.0886	0.0337	**0.0156**
	0.03	0.0345	0.0520	**0.0165**
Satellite	0.005	0.0550	0.0319	**0.0085**
	0.01	0.0597	0.0547	**0.0110**
	0.03	0.1090	0.1172	**0.0078**

see from the Table 2 that the NMSE values achieved by the proposed method are the lowest among the three methods for all noise levels, which means that the PSFs estimated by the proposed method are closer to the original PSFs. This validates the effectiveness of the proposed method.

Figs. 2–4 show the image deconvolution results under three different intensity noise levels for the Cameraman image. The blurred and noisy images, shown in Figs. 2(a), 3(a), and 4(a), were obtained by adding Gaussian blur with fspecial ('gaussian',11,2.1) and they are then contaminated by Gaussian noise with standard deviations 0.005, 0.01, and 0.03. From Figs. 2(b), 3(b), and 4(b), it can be observed that the algorithm of Krishnan et al. can restore some details and suppress the noise with a low noise level, but the noise amplification is very apparent when the noise level increases. Obvious artifacts caused by noise can also be observed in Figs. 2(c), 3(c), and 4(c) obtained by the algorithm of Levin et al. The noise is effectively removed in Figs. 2(d), 3(d), and 4(d) by the proposed algorithm compared with those by the algorithms of Krishnan et al. and Levin et al., and the important structural details are preserved. The introduction of the reweighted strategy offers the proposed algorithm the ability to deal with high intensity noise, which leads to a better deconvolution performance.

The deconvolution results of Lena and Satellite images for three different noise levels are also presented in Figs. 5–10. We can see

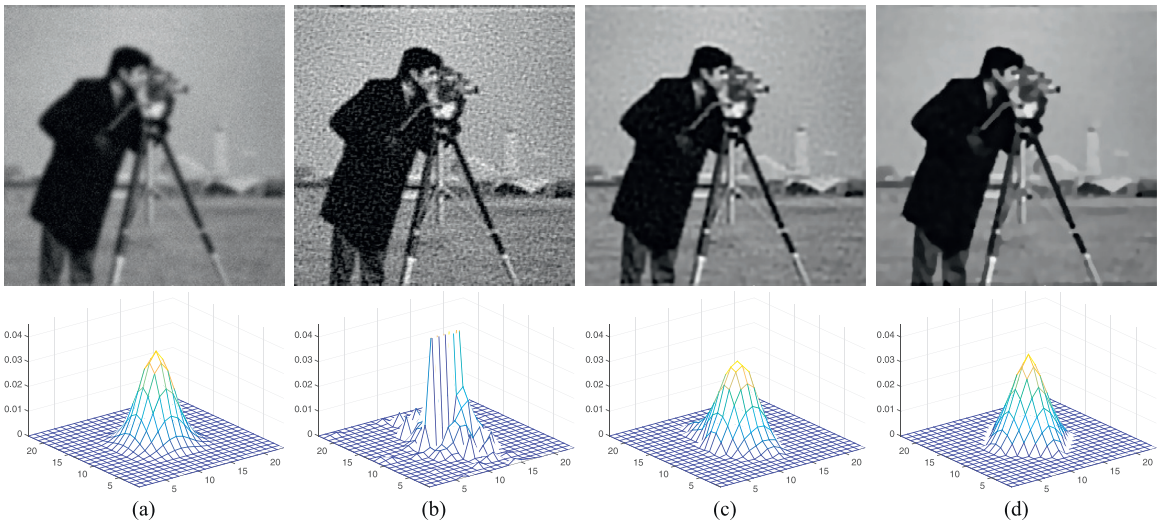


Fig. 4. Blind deconvolution results for the Cameraman image with the noise level = 0.03. (a) Image blurred by fspecial ('gaussian',11,2.1) and contaminated by Gaussian noise with standard deviation 0.03. Deconvolution results achieved using (b) Krishnan et al.'s algorithm [16], (c) Levin et al.'s algorithm [17], (d) our method. The bottom line: the original PSF and the estimated PSFs by three methods.

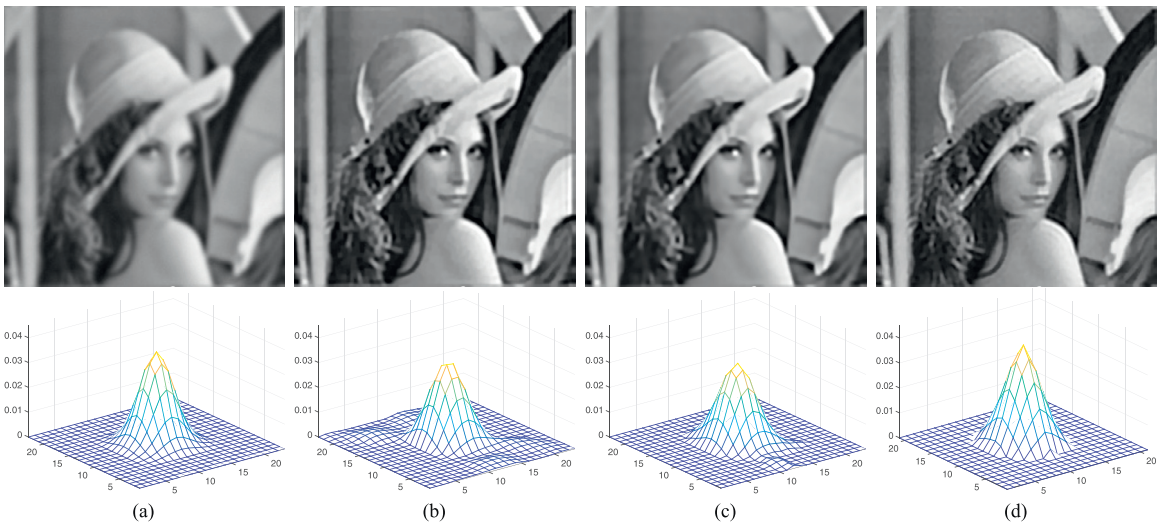


Fig. 5. Blind deconvolution results for the Lena image with the noise level = 0.005. (a) Image blurred by fspecial ('gaussian',11,2.1) and contaminated by Gaussian noise with standard deviation 0.005. Deconvolution results achieved using (b) Krishnan et al.'s algorithm [16], (c) Levin et al.'s algorithm [17], (d) our method. The bottom line: the original PSF and the estimated PSFs by three methods.

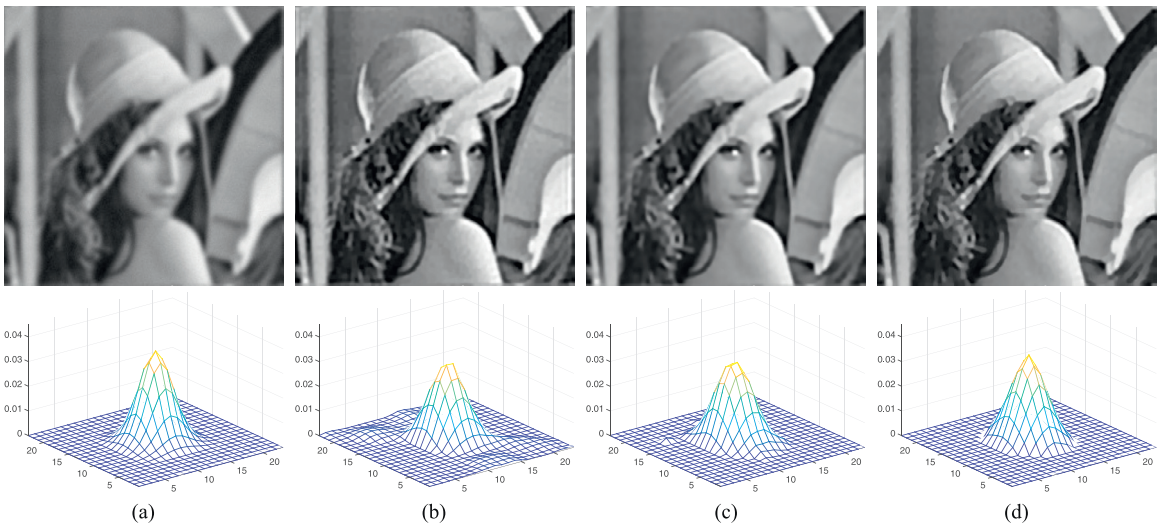


Fig. 6. Blind deconvolution results for the Lena image with the noise level = 0.01. (a) Image blurred by fspecial ('gaussian',11,2.1) and contaminated by Gaussian noise with standard deviation 0.01. Deconvolution results achieved using (b) Krishnan et al.'s algorithm [16], (c) Levin et al.'s algorithm [17], (d) our method. The bottom line: the original PSF and the estimated PSFs by three methods.

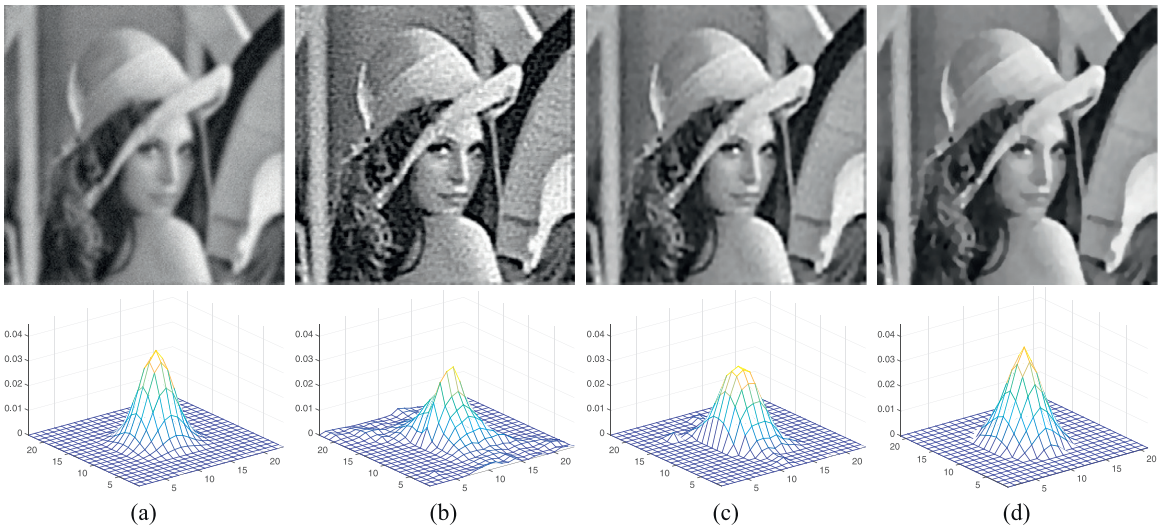


Fig. 7. Blind deconvolution results for the Lena image with the noise level = 0.03. (a) Image blurred by fspecial ('gaussian',11,2.1) and contaminated by Gaussian noise with standard deviation 0.03. Deconvolution results achieved using (b) Krishnan et al.'s algorithm [16], (c) Levin et al.'s algorithm [17], (d) our method. The bottom line: the original PSF and the estimated PSFs by three methods.

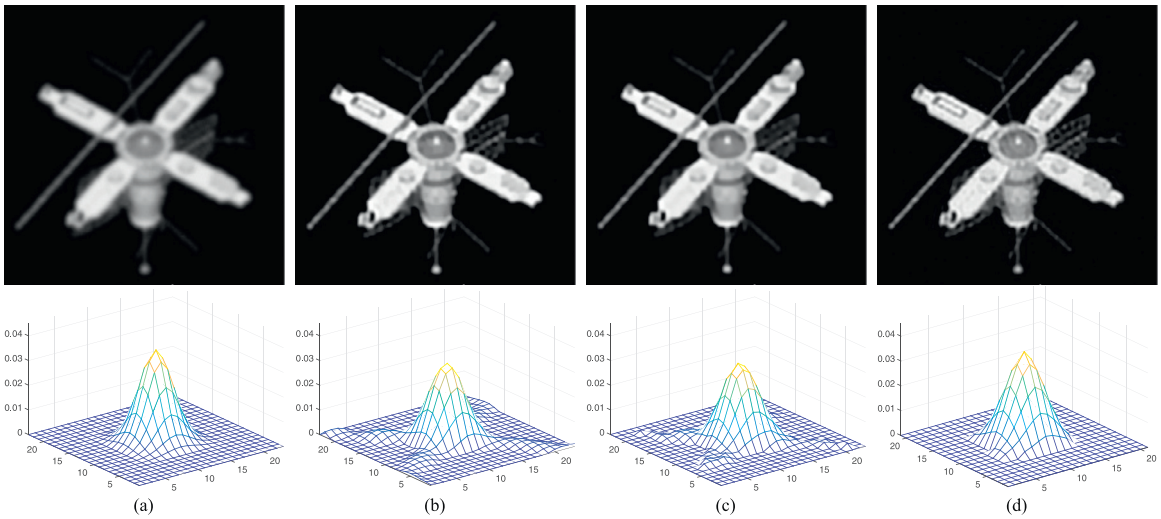


Fig. 8. Blind deconvolution results for the Satellite image with the noise level = 0.005. (a) Image blurred by fspecial ('gaussian',11,2.1) and contaminated by Gaussian noise with standard deviation 0.005. Deconvolution results achieved using (b) Krishnan et al.'s algorithm [16], (c) Levin et al.'s algorithm [17], (d) our method. The bottom line: the original PSF and the estimated PSFs by three methods.

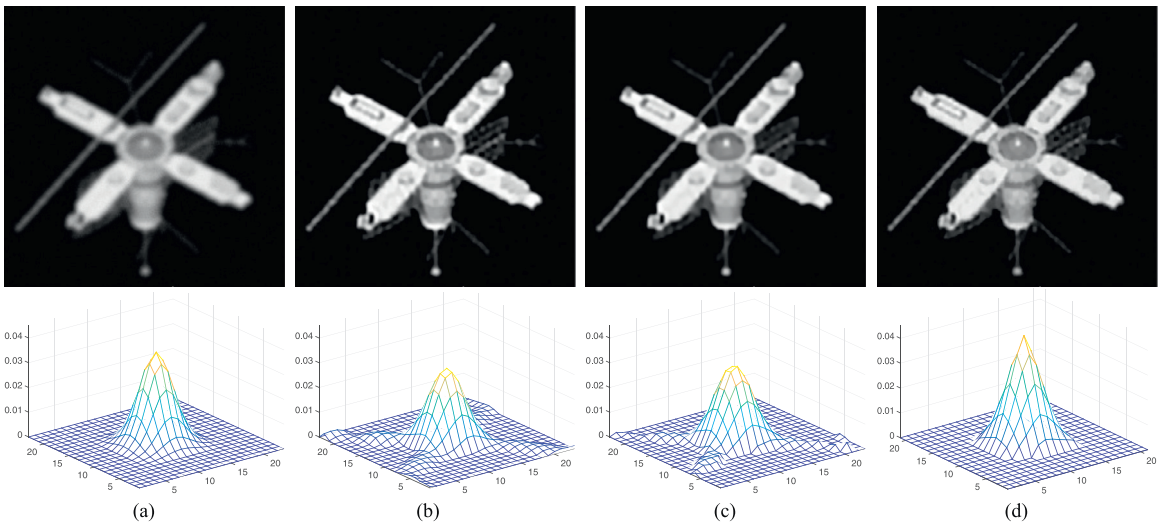


Fig. 9. Blind deconvolution results for the Satellite image with the noise level = 0.01. (a) Image blurred by fspecial ('gaussian',11,2.1) and contaminated by Gaussian noise with standard deviation 0.01. Deconvolution results achieved using (b) Krishnan et al.'s algorithm [16], (c) Levin et al.'s algorithm [17], (d) our method. The bottom line: the original PSF and the estimated PSFs by three methods.

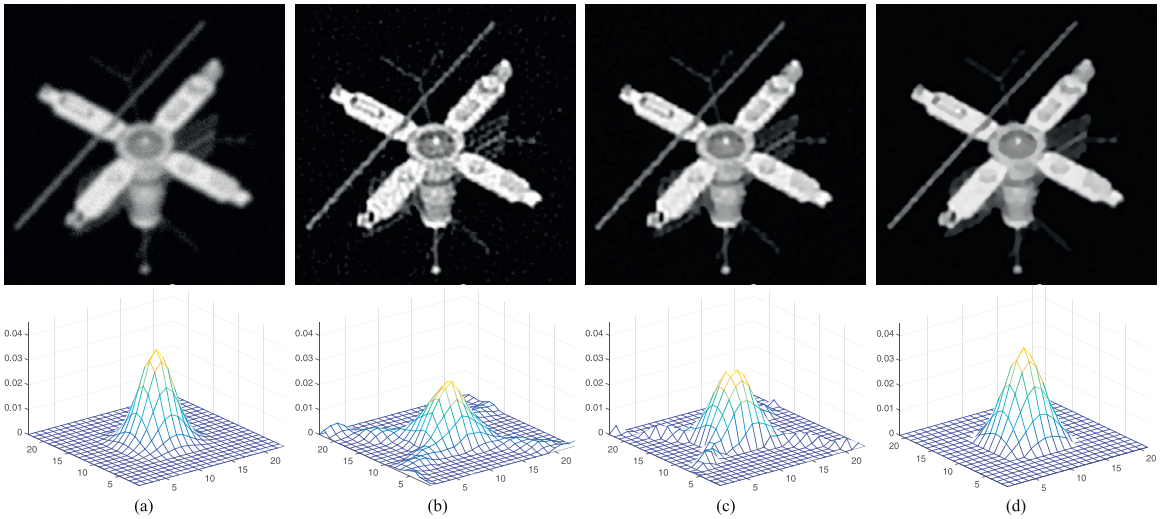


Fig. 10. Blind deconvolution results for the Satellite image with the noise level = 0.03. (a) Image blurred by fspecial ('gaussian',11,2.1) and contaminated by Gaussian noise with standard deviation 0.03. Deconvolution results achieved using (b) Krishnan et al.'s algorithm [16], (c) Levin et al.'s algorithm [17], (d) our method. The bottom line: the original PSF and the estimated PSFs by three methods.

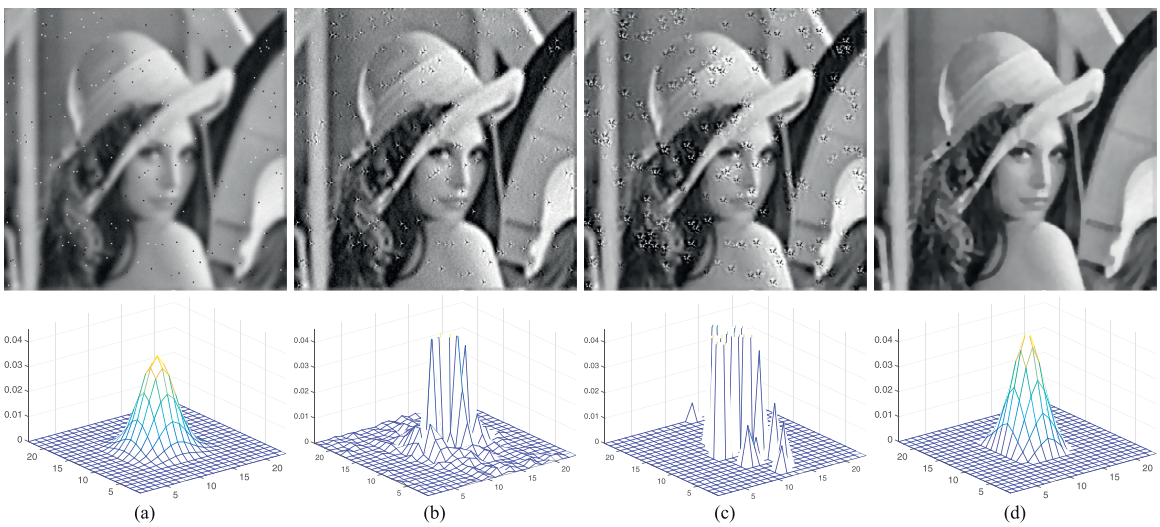


Fig. 11. Blind deconvolution results for the Lena image. (a) Image blurred by fspecial ('gaussian',11,2.1) and contaminated by Gaussian noise with standard deviation 0.01 and Salt-Pepper noise (noise density=0.004) (PSNR = 21.76 dB, SSIM = 0.6335). Deconvolution results achieved using (b) Krishnan et al.'s algorithm [16] (PSNR = 16.72 dB, SSIM = 0.5599), (c) Levin et al.'s algorithm [17] (PSNR = 20.55 dB, SSIM = 0.5835), (d) our method (PSNR = 25.62 dB, SSIM = 0.8027). The bottom line: the original PSF and the estimated PSFs by three methods.

that the proposed algorithm has a stable deconvolution performance for the Lena image and the Satellite image even though these images have different structural features. Additionally, as shown in these estimated PSFs, the PSFs obtained from the proposed method are more faithful to the original PSFs while the results of Krihsnan et al. and Levin et al. exhibit small errors.

To demonstrate the effectiveness of the proposed blind deconvolution method in the presence of mixed noise, we present two simulated experiments for the Lena image. In the first experiments, the original image is obtained by adding Gaussian blur with fspecial ('gaussian',11,2.1) and then contaminated by Gaussian noise with standard deviations 0.01 and salt-pepper noise (noise intensity 0.004). As shown in Figs. 11(b) and 11(c), the salt-pepper noise is obviously amplified and the estimated PSFs deviate from the original PSFs. The proposed method remarkably removes the mixed noise and preserves the details shown in Fig. 11(d), indicating that the proposed adaptive reweighted method is insensitive to mixed noise and can estimate a more accurate PSF. In the second experiment, the original image is obtained by adding Gaussian blur with fspecial ('gaussian',11,2.1) and then contaminated by Gaussian noise with standard deviations 0.01 and Poisson noise. In order to add Poisson noise to the original image, we first scaled the image by $(I_{\max}/\mathbf{x}_{\max})/10^{12}$, where $\mathbf{x}_{\max}$ is the maximal value of $\mathbf{x}$ and $I_{\max}$ is a specified maximal intensity (which coincides with the Poisson noise intensity). Then, we applied the MATLAB command imnoise(I, 'Poisson') and, scaled it back again as presented in [42]. As the Figs. 12(b) and (c) show, although the mixed noise is suppressed to some extent, some obvious noise artifacts are introduced. We can observe again that the estimated PSFs using the algorithms of Krishnan et al. and Levin et al. are not consistent with the original PSFs. Specifically, the PSF obtained by the Levin et al.'s algorithm is greatly deviated from the true PSF. As shown in Fig. 12(d), the results produced by the proposed method are still very nice for the two challenging examples under Gaussian and Poisson noise where a more accurate PSF is obtained. This confirms the robustness of the proposed method using the iteratively reweighted scheme. The reweighted strategy provides a convenient choice to flexibly incorporate an adaptive mechanism that makes

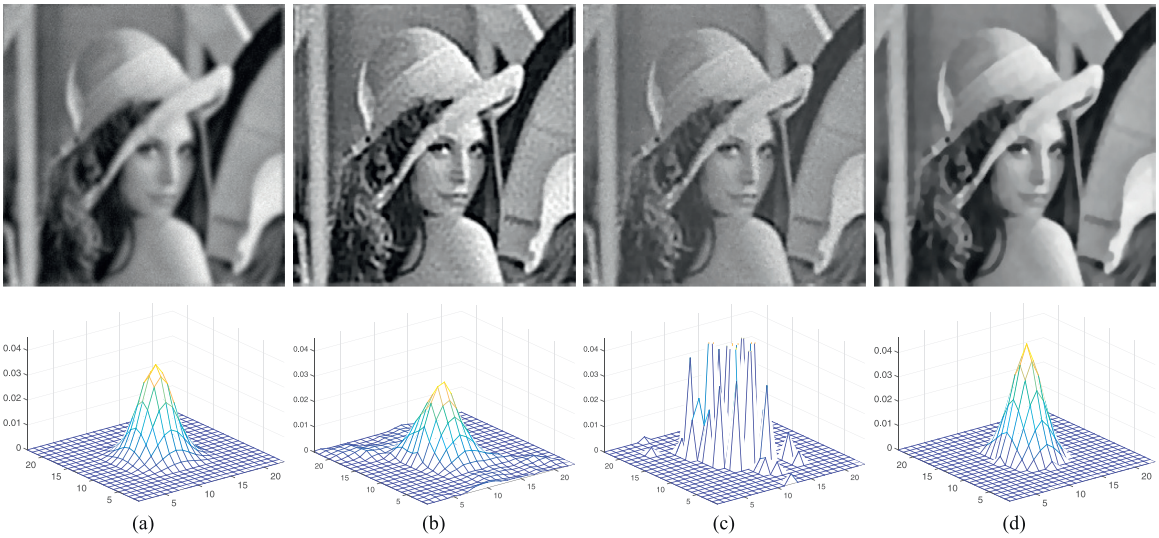


Fig. 12. Blind deconvolution results for the Lena image. (a) Image blurred by fspecial ('gaussian',11,2.1) and contaminated by Gaussian noise and Poisson noise (PSNR=22.50 dB, SSIM = 0.6170). Deconvolution results achieved using (b) Krishnan et al.'s algorithm [16] (PSNR=23.12 dB, SSIM=0.6891), (c) Levin et al.'s algorithm [17] (PSNR = 23.66 dB, SSIM = 0.6683), (d) our method (PSNR = 24.84 dB, SSIM = 0.7760). The bottom line: the original PSF and the estimated PSFs by three methods.

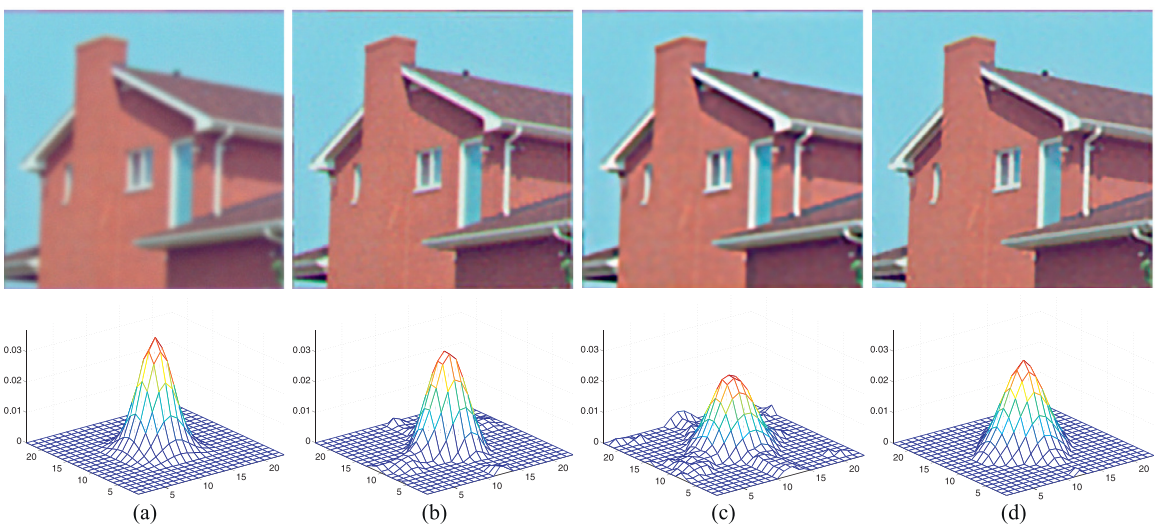


Fig. 13. Blind deconvolution results for the color House image. (a) Image blurred by fspecial ('gaussian',11,2.1) and contaminated by Gaussian noise with standard deviation 0.01 (PSNR = 24.54 dB). Deconvolution results achieved using (b) Krishnan et al.'s algorithm [16] (PSNR = 26.50 dB), (c) Levin et al.'s algorithm [17] (PSNR = 27.22 dB), (d) our method (PSNR = 29.32 dB). The bottom line: the original PSF and the estimated PSFs by three methods.

the model robust to mixed noise. From the two experiments, we can find that the proposed method also achieves higher PSNR and SSIM values than the other two methods.

To demonstrate the effectiveness of the proposed blind deconvolution method for the color image, we present a simulated experiment for the color House image. The image is blurred by fspecial ('gaussian',11,2.1) and contaminated by Gaussian noise with standard deviation 0.01 (See Fig. 13 (a)). The results presented in Fig. 13(b)–(d) demonstrated that the proposed method can be also adopted to restore the color image and obtain a satisfactory restoration result from the quantitative and visual evaluation.

B. Real PMMW image blind deconvolution experiments

Because of the long wavelength of the millimeter-wave and the limitation of antenna aperture size, the PMMW image often suffers low spatial resolution. In addition, the observed image is inevitably polluted by noise. Blind deconvolution is used to improve the spatial resolution and suppress the noise. In this subsection, we present the capability of the proposed blind deconvolution method for real images captured by a 94 GHz PMMW radiometer. Figs. 14(a) and 16(a) are captured by our 94 GHz PMMW mechanically scanned radiometer at two different scenes. Fig. 15(a) is taken with a 94 GHz PMMW radiometer at the London Heathrow airport [43].

Figs. 14(a), 15(a), and 16(a) are three original observed PMMW images in an outdoors environment. Figs. 14(b), 15(b), and 16(b) are the results obtained by Krisnan et al.'s method, in which evident artifacts induced by noise can be seen and the details are almost covered due to amplified noise. Figs. 14(c), 15(c), and 16(c) show the results achieved by Levin et al.'s method, where the noise is suppressed well. However, it appears that the image is oversmooth and the high brightness area is oversaturated, such as the light area as shown in Fig. 16(b). The resulting images by the proposed method are shown in Figs. 14(d), 15(d), and 16(d). We can observe that our method can remove the image noise to a large extent while recovering the image detail information. One can observe that the proposed method can produce the smoother PSFs,

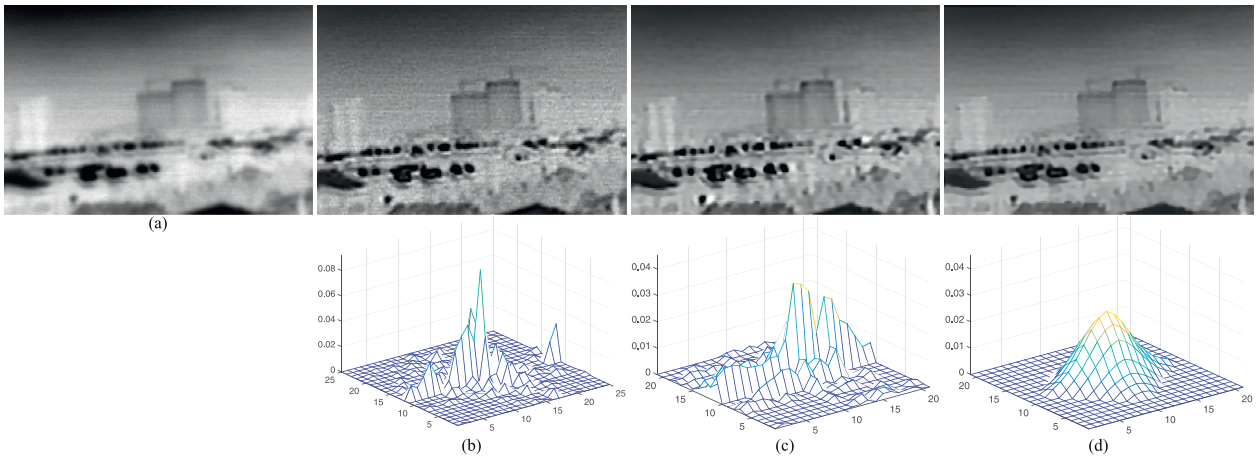


Fig. 14. Blind deconvolution for real PMMW image. (a) PMMW image captured by 94 GHz mechanically scanned PMMW radiometer. Results obtained by (b) Krishnan et al.'s algorithm [16], (c) Levin et al.'s algorithm [17], (d) our method.

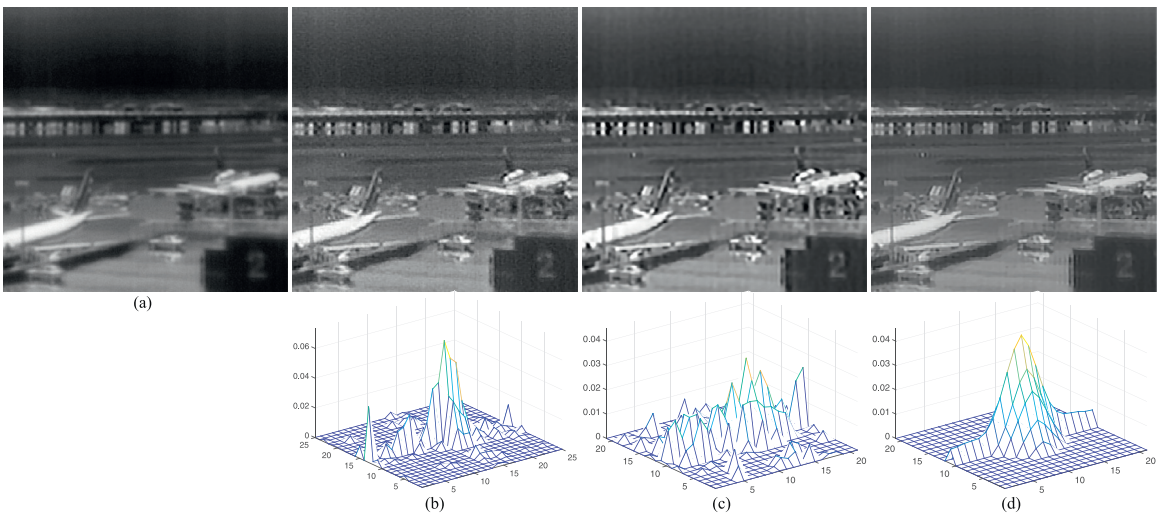


Fig. 15. Blind deconvolution for real PMMW image. (a) 94 GHz image obtained by the Defence Evaluation Research Agency, Malvern, UK. Results obtained by (b) Krishnan et al.'s algorithm [16], (c) Levin et al.'s algorithm [17], (d) our method.

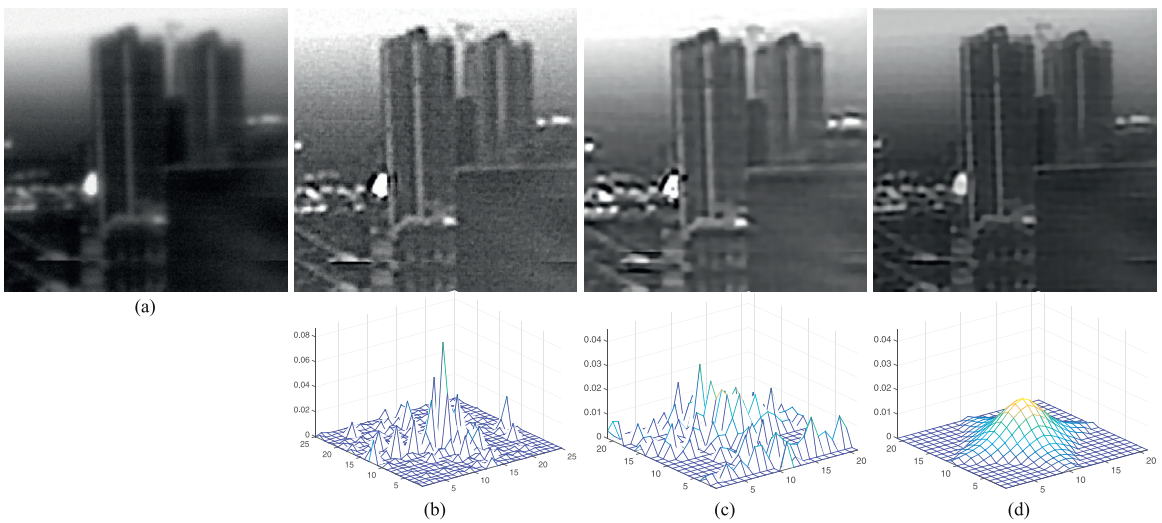


Fig. 16. Blind deconvolution for real PMMW image. (a) PMMW image captured by 94 GHz mechanically scanned PMMW radiometer. Results obtained by (b) Krishnan et al.'s algorithm [16], (c) Levin et al.'s algorithm [17], (d) our method.

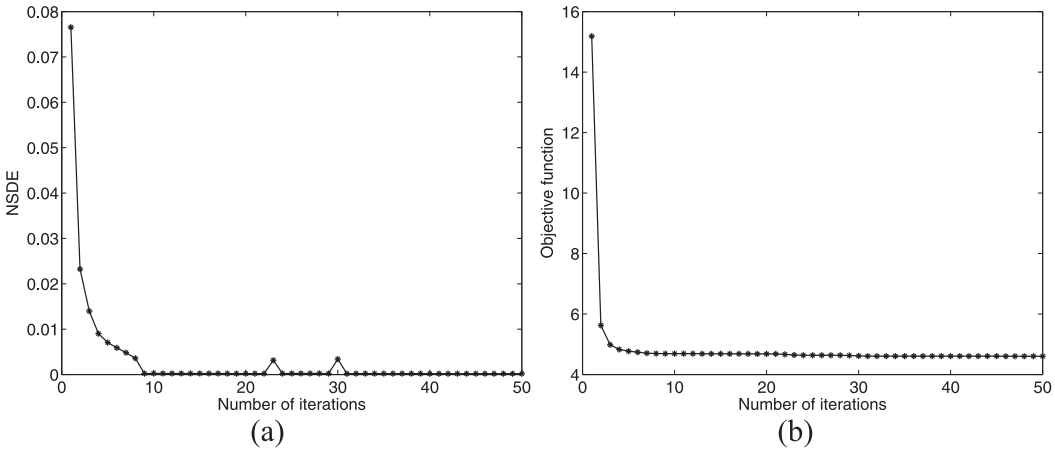


Fig. 17. Evolution of functional energy versus number of iterations for the proposed method.

Table 3
Calculating time (in unit of: seconds) of three methods on real images.

Image	Size	Krishnan et al. [16]	Levin et al. [17]	Proposed
Factory	230 × 340	23.94	418.63	24.41
Airport	384 × 384	41.13	443.29	89.72
Building	256 × 256	20.26	389.56	22.22

while the other two methods obtain the irregular PSFs with many uneven peaks.

Furthermore, the computational time of the Krishnan et al.'s method, Levin et al.'s method, and the proposed method on real images is listed in Table 3. All experiments are conducted in Matlab 2014b environment on a Dell OPTIPLEX 9020 computer with Intel(R) Core(TM) i7-4790 CPU (3.6 GHz), 8GB memory, and Windows 7 operating system. From Table 3, we can see that Krishnan et al.'s method has the lowest computational load while the Levin et al.'s method takes the most computational time among the three methods.

3.1. Convergence rate of the algorithm

We investigated the convergence behavior of the proposed method. Fig. 17(a) and (b) illustrate the evolution of the normalized step difference energy (NSDE) (NSDE= $\|\mathbf{x}^{k+1}-\mathbf{x}^{k}\|_2/\|\mathbf{x}^{k}\|_2$) and the energy functional versus the number of iterations for Lena image, which is blurred by Gaussian kernel with Matlab function fspecial (gaussian,11,2.1) and contaminated by Gaussian noise with standard deviation 0.01 (see Fig. 6). It can be seen clearly that the proposed method achieves good convergence and converges after about 10 iterations.

4. Conclusion

In this paper, we study the problem of image blind deconvoloution for PMMW images. We present a weighted objective function which consists of a weighted data-fidelity term, a weighted BTV regularization term for the image, and a smooth term for the PSF. The weighted data-fidelity term has the ability to deal with mixed noise and the weighted BTV regularization term can preserve the important image structure. The smooth PSF constraint favors an accurate PSF estimation. The final reweighted function can be solved by the scaled CG method or preconditioned CG method. The proposed algorithm produces high quality reconstruction images in terms of both PSNR and SSIM values and visual effect. The regularization parameters for the proposed approach are estimated from an approximate formula automatically.

Acknowledgments

This work was supported by the National Natural Science Foundation of China under Grant 41501371. The authors are grateful to the associate editor Dr. Dacheng Tao and the reviewers for their time and the valuable suggestions and Dr. Ming Zhang for correcting the grammatical errors, the paper is better because of your efforts. We also thank Dr. P. R. Coward, QinetiQ Malvern UK, for the use of the Heathrow airport image.

References

[1] L. Yujiri, M. Shoucri, P. Moffa, Passive millimeter-wave imaging, IEEE Microw. Mag. 4 (3) (2003) 39–50.
[2] H. Fang, L. Yan, T. Zhang, H. Liu, M. Jin, Parametric blind deconvolution for passive millimeter wave images basing on image decomposition, in: Proc. of 2011 SPIE, 8002, 2011. 80021K(1)–80021K(8)
[3] H. Fang, L. Yan, Parametric blind deconvolution for passive millimeter wave images with framelet regularization, Optik 125 (2014) 1454–1460.
[4] Q. Zhao, L. Zhang, A. Cichocki, Bayesian cp factorization of incomplete tensors with automatic rank determination, IEEE Trans. Pattern Anal. Mach. Intell. 37 (9) (2015) 1751–1763.
[5] Y. Wang, C. Xu, S. You, D. Tao, C. Xu, Parts for the whole: the dct norm for extreme visual recovery, CoRR (2016). abs/1604.05451.
[6] Y.A. Pirogov, V.V. Gladun, D.A. Tischenko, A.L. Timanovskiy, I.V. Shlemin, S.F. Cheng, Passive millimeter-wave imaging with superresolution, in: Proc. of SPIE, Image and Signal Processing for Remote Sensing X, 5573, 2004, pp. 72–83.
[7] M.K. Singh, H. Park, S.-H. Kim, U.S. Tiwary, Y.-H. Kim, Linear and nonlinear methods for passive millimeter-wave image deblurring, in: 25th Anniversary IGARSS 2005: IEEE international Geoscience and Remote Sensing Symposium, 5, 2005, pp. 3685–3688.
[8] H. Park, S.-H. Kim, M.K. Singh, J.-H. Choi, H.-J. Lee, Y.-H. Kim, Performance analysis of wavelet based restoration for passive millimeter-wave images, in: Proc. of SPIE, 5789, 2005, pp. 157–166.
[9] B. Amizic, L. Spinoulas, R. Molina, A.K. Katsaggelos, Compressive blind image deconvolution, IEEE Trans. Image Process. 22 (10) (2013) 3994–4006.
[10] W. AlSaafin, S. Villena, M. Vega, R. Molina, A.K. Katsaggelos, Compressive sensing super resolution from multiple observations with application to passive millimeter wave images, Digital Signal Process. 50 (2016) 180–190.
[11] H. Park, M.K. Singh, S.-H. Kim, H.-J. Lee, Y.-H. Kim, Blind image restoration for mmw radiometer based on wavelet techniques, in: Proceedings of 2005 IEEE International Geoscience and Remote Sensing Symposium (IGARSS), 6, 2005, pp. 4279–4282.
[12] H. Fang, L. Yan, H. Liu, Y. Chang, Blind poissonian images deconvolution with framelet regularization, Opt. Lett. 38 (4) (2013) 389–391.
[13] M. Renu, S. Chaudhuri, R. Velmurugan, Convergence analysis of a quadratic upper bounded TV regularizer based blind deconvolution, Signal Process. 106 (2015) 174–183.
[14] Y. Ruan, H. Fang, Q. Chen, Semiblind image deconvolution with spatially adaptive total variation regularization, Math. Prob. Eng. 2014 (2014) 1–8.
[15] Y. Li, J. Archer, J. Tello, G. Rosolen, F. Ceccato, S. Hay, A. Hellicar, Y. Guo, Performance evaluation of a passive millimeter-wave imager, IEEE Trans. Microw. Theory Technol. 57 (10) (2009) 2391–2405.
[16] D. Krishnan, T. Tay, R. Fergus, Blind deconvolution using a normalized sparsity measure, in: 2011 IEEE Conference on Computer Vision and Pattern Recognition, 2011, pp. 233–240.

[17] A. Levin, Y. Weiss, F. Durand, W. Freeman, Efficient marginal likelihood optimization in blind deconvolution, in: 2011 IEEE Conference on Computer Vision and Pattern Recognition, 2011, pp. 2657–2664.
[18] S.J. Reeves, An analysis of the difficulties and possibilities for superresolution, in: Proc. of SPIE, 3064, 1997, pp. 239–248.
[19] P. Rodríguez, B. Wohlberg, Efficient minimization method for a generalized total variation functional, IEEE Trans. Image Process. 18 (2) (2009) 322–332.
[20] B. Calef, Iteratively reweighted blind deconvolution, Proceedings of 2013 IEEE International Conference on Image Processing(ICIP), Melbourne, VIC, 2013, pp. 1391–1393.
[21] T. Köhler, X. Huang, F. Schebesch, A. Aichert, A. Maier, J. Hornegger, Robust multiframe super-resolution employing iteratively re-weighted minimization, IEEE Trans. Comput. Imaging 2 (1) (2016) 42–58.
[22] S. Farsiu, M. Robinson, M. Elad, P. Milanfar, Fast and robust multi-frame super resolution, IEEE Trans. Image Process. 13 (10) (2004) 1327–1344.
[23] E.J. Candes, M.B. Wakin, S.P. Boyd, Enhancing sparsity by reweighted ℓ_1 minimization, J. Fourier Anal. Appl. 14 (5) (2008) 877–905.
[24] D. Wipf, H. Zhang, Revisiting bayesian blind deconvolution, J. Mach. Learn. Res. 15 (2014) 3595–3634.
[25] L. Wang, L. Xiao, J. Zhang, Z. Wei, New image restoration method associated with tetrolets shrinkage and weighted an isotropic total variation, Signal Process. 93 (4) (2013) 661–670.
[26] W. Dong, L. Zhang, G. Shi, Centralized sparse representation for image restoration, in: IEEE International Conference on Computer Vision, 2011, pp. 1259–1266.
[27] T. Liu, D. Tao, Classification with noisy labels by importance reweighting, IEEE Trans. Pattern Anal. Mach. Intell. 38 (3) (2016) 447–461.
[28] T.F. Chan, S. Esedoglu, Aspects of total veriation regularized l1 function approximation, SIAM J. Appl. Math. 35 (5) (2005) 1817–1837.
[29] I.T. Nabney, NETLAB: Algorithms for Pattern Recognition, Springer, 2002.
[30] M. Kang, A. Katsaggelos, General choice of the regularization functional in regularized image-restoration, IEEE Trans. Image Process. 4 (5) (1995) 594–602.
[31] Y.-R. Li, L. Shen, D.-Q. Dai, B.W. Suter, Framelet algorithms for de-blurring images corrupted by impulse plus gaussian noise, IEEE Trans. Image Process. 20 (7) (2011) 1822–1837.
[32] A. Mohammad-Djafari, Joint estimation of parameters and hyperparameters in a bayesian approach of solving inverse problems, in: Proceedings of 1996 IEEE International Conference on Image Processing(ICIP), 1996. 473–472.
[33] A. Mohammad-Djafari, A Full Bayesian Approach for Inverse Problems, in: K. Hanson, R. Silver (Eds.), Maximum Entropy and Bayesian Methods, 79, Kluwer, 1996, pp. 135–144.
[34] J.H. Money, S.H. Kang, Total variation minimizing blind deconvolution with shock filter reference, Image Vis. Comput. 26 (2) (2008) 302–314.
[35] S. Cho, S. Lee, Fast motion deblurring, ACM Trans. Graph. 28 (5) (2009) 145:1–145:8.
[36] E. Faramarzi, D. Rajan, M.P. Christensen, Unified blind method for multi-image super-resolution and single/multi-image blur deconvolution, IEEE Trans. Image Process. 2 (6) (2013) 2101–2114.
[37] L. Xu, C. Lu, Y. Xu, J. Jia, Image smoothing via L0 gradient minimization, ACM Trans. Graph. 30 (6) (2011) 174:1–174:11.
[38] D. Perrone, P. Favaro, Total variation blind deconvolution: The devil is in the details, in: 2014 IEEE Conference on Computer Vision and Pattern Recognition, 2014, pp. 2909–2916.
[39] D. Perrone, P. Favaro, A logarithmic image prior for blind deconvolution, Int. J. Comput. Vis. 117 (2) (2015) 159–172.
[40] I. Nabney, Netlab toolbox (2002). www.ncrg.aston.ac.uk/netlab/index.html.
[41] Z. Wang, A.C. Bovik, H.R. Sheikh, E.P. Simoncelli, Image quality assessment: from error visibility to structural similarity, IEEE Trans. Image Process. 13 (4) (2004) 600–612.
[42] H. Fang, L. Yan, Poissonian image deconvolution with analysis sparsity priors, J. Electron. Imaging 22 (2) (2013) 023033(1)–023033(10).
[43] P.R. Coward, R.N. Anderton, S. Price, Receiver array design for conically scanned millimetre-wave imagers, in: Proceedings of SPIE (2004), 5619, 2004, pp. 108–116.